

SDSSJ0018-0939: A Clear Signature of Sub-Chandrasekhar Mass Type 1a Supernova

S. K. Jeena,^{1*} and Projjwal Banerjee^{1†}

¹*Department of Physics, Indian Institute of Technology Palakkad, Kerala, India*

ABSTRACT

Very metal-poor (VMP) stars ($[\text{Fe}/\text{H}] \leq -2$) that have sub-solar values of $[\text{X}/\text{Fe}]$ for α elements such as Mg, Si, and Ca, are referred to as α -poor VMP stars. They are quite rare among VMP stars and are thought to have formed from gas enriched predominantly by a single Type Ia supernovae (SN 1a) in contrast to most VMP stars which are α -enhanced and usually associated with core-collapse supernovae. The observed abundance pattern in such stars can provide a direct way to probe the nucleosynthesis in individual SN 1a. Although the abundance patterns in some α -poor VMP stars have been shown to be consistent with SN 1a ejecta, a clear nucleosynthetic signature for SN 1a resulting from the explosion of a near Chandrasekhar mass (near- M_{Ch}) or a sub-Chandrasekhar mass (sub- M_{Ch}) white dwarf, has not been unambiguously detected. We perform a detailed analysis of various formation channels of VMP stars and find that the α -poor VMP star SDSSJ0018-0939, which was earlier reported as a star with potential pair-instability supernova origin, provides almost a smoking-gun signature of a sub- M_{Ch} SN 1a resulting from He detonation. We find that compared to other α -poor VMP stars that were previously identified with SN 1a, SDSSJ0018-0939 is the only star that has a clear and unambiguous signature of SN 1a. Interestingly, our results are consistent with constraints on SN 1a from recent galactic chemical evolution studies that indicate that sub- M_{Ch} SN 1a account for ~ 50 – 75 % of all SN 1a and possibly the dominant channel in the early Galaxy.

Key words: stars: massive – stars: Population III – stars: Population II – stars: abundances – stars: chemically peculiar – nuclear reactions, nucleosynthesis, abundances

1 INTRODUCTION

Studying very metal-poor (VMP) stars with metallicity $[\text{Fe}/\text{H}] < -2$ is crucial for understanding the evolution of elements in the early Galaxy during the first billion years after the Big Bang (Beers & Christlieb 2005; Frebel & Norris 2015). The majority of VMP stars exhibit an enhanced abundance of α elements such as C, O, Mg, Si, and Ca with super-solar values of $[\text{X}/\text{Fe}]$ (Cayrel et al. 2004). These stars are thought to have formed from gas polluted by core-collapse supernovae (CCSNe), and their detailed abundance pattern can be explained by the mixing and fallback of CCSN ejecta (Umeda & Nomoto 2003, 2005; Heger & Woosley 2010; Tominaga et al. 2014). On the other hand, VMP stars that have $[\text{X}/\text{Fe}] < 0$ for Mg and most α elements, are known as α -poor VMP stars and are quite rare among VMP stars. Their peculiar abundance pattern is typically associated with gas polluted by SN 1a (Ivans et al. 2003; Li et al. 2022) as nucleosynthesis in SN 1a models naturally produces negligible Mg along with sub-solar values of $[\text{X}/\text{Fe}]$ for α elements.

In this regard, it is important to note that the nature of progenitors as well as the mechanism of explosion for SN 1a are subjects of ongoing debate, as successful explosions from first principles are still lacking in numerical simulations. Broadly, the scenarios proposed are associated with the explosion of a white dwarf (WD) in a binary

configuration with a red giant star (single degenerate) or with another WD (double degenerate). The proposed explosion mechanism includes pure detonation, pure deflagration, and delayed detonation (deflagration to detonation) for near-Chandrasekhar mass (near- M_{Ch}) models along with double detonation for sub-Chandrasekhar mass (sub- M_{Ch}) models. The explosion mechanisms and nucleosynthesis resulting from the various scenarios have been extensively studied over the last several decades (Nomoto et al. 1984; Woosley et al. 1986; Khokhlov 1991; Iwamoto et al. 1999; Woosley & Kasen 2011; Seitzzahl et al. 2013a; Fink et al. 2014; Leung & Nomoto 2018; Shen et al. 2018; Bravo 2019; Bravo et al. 2019; Leung & Nomoto 2020; Lach et al. 2020; Gronow et al. 2021). Among the various explosion mechanisms and scenarios that have been proposed, delayed detonation for near- M_{Ch} and double detonation for sub- M_{Ch} SN 1a are currently considered to be the dominant channels (Shen et al. 2018; Kirby et al. 2019). The relative frequency of near- M_{Ch} and sub- M_{Ch} models and their contribution to the galactic chemical evolution is one of the crucial questions that several recent studies have tried to constrain. By considering the chemical evolution of key elements such as Mn and Ni, several studies have found that a significant fraction of the contribution comes from sub- M_{Ch} SN 1a resulting from He detonations accounting for 50–70 % of all SN 1a (Seitzzahl et al. 2013b; Kirby et al. 2019; de los Reyes et al. 2020; Kobayashi et al. 2020; Eitner et al. 2020, 2023). Furthermore, some of these also suggest that sub- M_{Ch} SN 1a could even be more domi-

* E-mail: jeenaunni44@gmail.com

† E-mail: projjwal.banerjee@gmail.com

nant in the early Galactic evolution with near- M_{Ch} dominating in the later phases (Kirby et al. 2019).

An important implication of such findings is that many of the α -poor VMP stars should carry a clear signature of individual sub- M_{Ch} SN 1a. Detailed abundance in α -poor VMP stars can thus be used to confirm this and also provide direct evidence of the existence of sub- M_{Ch} SN 1a. Even though abundance patterns in some α -poor VMP stars have been analysed in detail and compared to theoretical SN 1a yields, a clear unambiguous match to the observed pattern is still lacking. The situation is made complicated by the fact that a recent study by Jeena et al. (2024) has pointed out that CCSNe, that do not undergo substantial fallback, can also result in patterns with sub-solar values of $[\text{Mg}/\text{Fe}]$ that can potentially match the pattern observed in some of the α -poor VMP stars. This makes the unambiguous association of an α -poor VMP star to an SN 1a even more challenging.

We identify a star named SDSSJ0018-0939, which exhibits the most prominent signature of being born from gas polluted by sub- M_{Ch} SN 1a resulting from He detonation. SDSSJ0018-0939 is a well-known chemically peculiar VMP star with metallicity $[\text{Fe}/\text{H}] = -2.5$, which has an elemental abundance pattern that is distinct from other VMP stars and was first reported by Aoki et al. (2014). The peculiar abundance pattern was interpreted by Aoki et al. (2014) as a possible signature of a star formed from a gas polluted by ejecta from a pair-instability SN (PISN). We find, however, that PISN provides a very poor fit to the observed abundance pattern and can be ruled out as the source of elements in SDSSJ0018-0939. Instead, we find that SDSSJ0018-0939 stands out as a unique star that shows the clearest signature of a sub- M_{Ch} SN 1a.

Our conclusion is based on a novel and detailed analysis that explores the various scenarios of the origin of elements in VMP stars. This includes enrichment from a PISN, a single CCSN, mixing of ejecta from two CCSNe, as well as the mixing of the ejecta from a CCSN and ejecta from both near- M_{Ch} and sub- M_{Ch} SN 1a. We consider a wide range of CCSN models that undergo mixing and fallback along with SN 1a from delayed detonation near- M_{Ch} models and double detonation sub- M_{Ch} models and use a χ^2 minimization to find the best-fit models. We find that other α -poor VMP stars such as COS171, BD+80245, HE0533-5340, and SMSSJ034249-284216, which have recently been identified with sub- M_{Ch} SN 1a (McWilliam et al. 2018; Reggiani et al. 2023), can also be fit well with purely CCSN models and thus cannot be unambiguously associated with SN 1a. In sharp contrast, SDSSJ0018-0939 has the clearest signature of a star that is formed from gas polluted dominantly by a sub- M_{Ch} SN 1a resulting from a He detonation. We identify key abundance features that make SDSSJ0018-0939 stand out among other α -poor VMP stars.

The structure of this paper is as follows: in Sec. 2, we discuss the theoretical models used in this study; Sec. 3 we discuss the details of the different scenarios for explaining abundance pattern in VMP stars and the methods used to find best-fit models. The results of the analysis for SDSSJ0018-0939 are discussed in Sec. 4 and the corresponding results for four other α -poor VMP stars in 5. Lastly, we finish with the summary and conclusion in Sec. 6.

2 THEORETICAL MODELS AND THE ABUNDANCE PATTERN

2.1 PISN models

We adopt the PISN models from Heger & Woosley (2002) that include the PISN yields from Pop III stars with He core masses ranging

from 65–130 M_{\odot} corresponding to zero-age main sequence mass of ~ 140 –260 M_{\odot} . Figure 1a shows the corresponding abundance patterns for some of the PISN models covering the progenitor mass range. As can be seen from the figure, the abundance pattern varies substantially with the He core mass. Lower He core PISN models of $\lesssim 90 M_{\odot}$ have a large overproduction of light and intermediate elements relative to Fe with a less pronounced odd-even effect. With increasing progenitor mass, the amount of Fe peak production increases dramatically due to explosive Si burning that leads to lower $[X/\text{Fe}]$ for elements lighter than Fe along with increased odd-even effect with highly sub-solar values for odd elements.

2.2 CCSN Models

We use a large adaptive co-processing network with reaction rates based on Rauscher et al. (2002) and follow the evolution of the star from birth to death via CCSN using the 1D hydrodynamic stellar evolution code KEPLER (Weaver et al. 1978; Rauscher et al. 2003). We consider non-rotating models of mass ranging from 10.1–30 M_{\odot} , as detailed in Jeena et al. (2024). The initial composition of these models is taken from Cyburt et al. (2002) that corresponds to primordial Big Bang nucleosynthesis. We refer to these as the z models.

The explosion is simulated by driving a piston from a mass coordinate, $M_{\text{cut,ini}}$, below which all the matter is assumed to fall back to the proto-neutron star. We consider two different choices of $M_{\text{cut,ini}}$ in this study, which is identical to Heger & Woosley (2010). In the first case, $M_{\text{cut,ini}}$ is chosen to be the mass coordinate where the entropy per baryon S exceeds $4 k_{\text{B}}$, which typically coincides with the base of the oxygen shell. In the second case, $M_{\text{cut,ini}}$ is chosen to be the mass coordinate at the edge of the iron core where there is a Y_{e} jump. We refer to the former as S_4 models and the latter as Y_{e} models. We use a nomenclature where we use the mass followed by the nature of the model (S_4 or Y_{e}) to clearly identify the various CCSN models. For example, a 15 M_{\odot} progenitor from S_4 model is referred to as $z15$ - S_4 . We consider explosion energies of 1.2×10^{51} erg and 1.2×10^{52} erg for all mass models. Lower mass progenitors of ~ 10 –12 M_{\odot} are found to have explosion energies of $\lesssim 10^{51}$ erg from detailed 3D simulations (Müller et al. 2019). To explore this, we also consider explosion energies of 0.3×10^{51} erg and 0.6×10^{51} erg for all progenitors of initial mass $< 12 M_{\odot}$. The ejecta for each SN explosion is calculated using the mixing and fallback model identical to Jeena et al. (2023) and Jeena et al. (2024) which are based on the models described in Tominaga et al. (2007); Ishigaki et al. (2014). In this model, following the explosive nucleosynthesis by the SN shock, all material above a mass coordinate $M_{\text{cut,fin}}$ is fully ejected, whereas a fraction f_{cut} , of the material between $M_{\text{cut,ini}}$ and $M_{\text{cut,fin}}$ is ejected. $M_{\text{cut,fin}}$ and f_{cut} , are treated as free parameters, whereas the value of $M_{\text{cut,ini}}$ is fixed as mentioned above. The value of $M_{\text{cut,fin}}$ is varied in steps of 0.1 M_{\odot} , starting from a minimum value of $M_{\text{cut,ini}}$ to a maximum value that corresponds to the base of the H envelope. The value of f_{cut} varied between 0 to 1. Thus, the amount of any isotope ejected by the SN for each model depends on the values of $M_{\text{cut,fin}}$ and f_{cut} . In this case, $\Delta M_{\text{fb}} = (1 - f_{\text{cut}})\Delta M_{\text{cut}}$ is the amount of matter that falls back to the compact remnant, where $\Delta M_{\text{cut}} = M_{\text{cut,fin}} - M_{\text{cut,ini}}$.

The nucleosynthesis of elements in massive stars involves a complex sequence of nuclear reactions during various stages of stellar evolution along with explosive nucleosynthesis during SN explosion as discussed in detail in Woosley et al. (2002); Heger & Woosley (2010) and more recently in Jeena et al. (2024). The final abundance pattern depends on the explosion energy and mass of the progenitor along with the details of mixing and fallback. However, as shown in

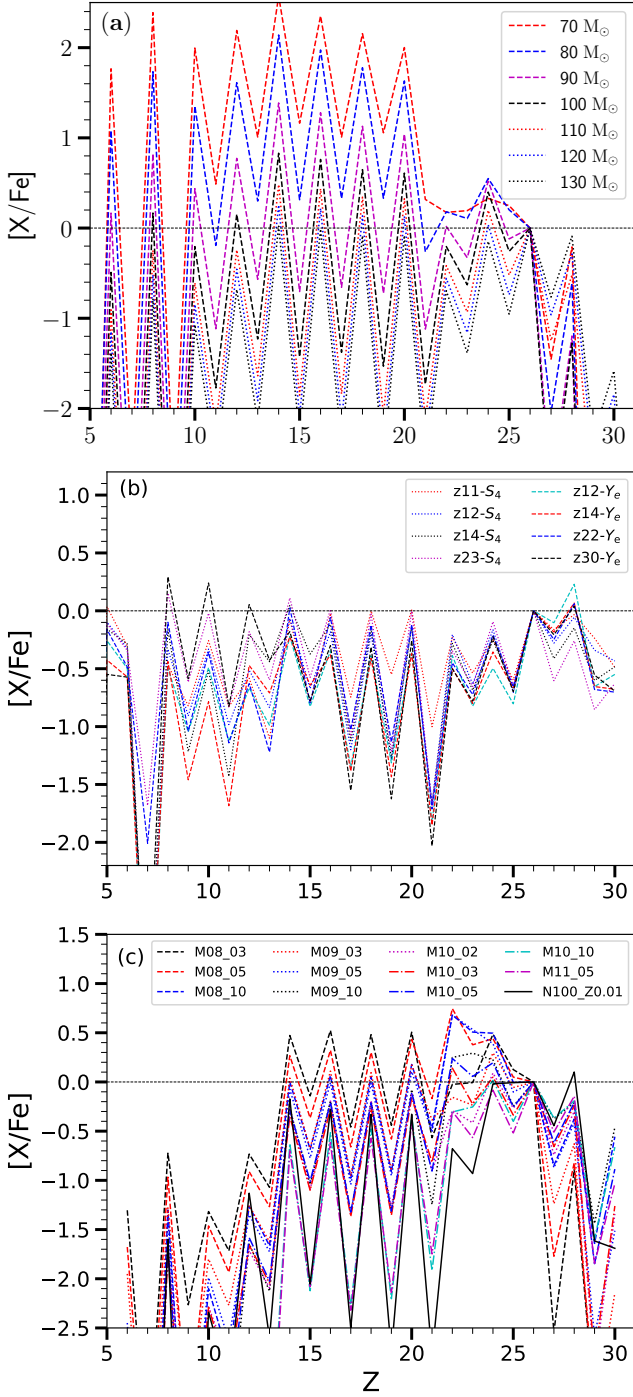


Figure 1. Theoretical elemental pattern relative to Fe from various sources. (a) PISN models from Heger & Woosley (2002), labelled with the corresponding He core mass. (b) CCSN ejecta for z models of 10.1–30 M_{\odot} without mixing and fallback, and have values of $[\text{Mg}/\text{Fe}] \lesssim 0.0$. (c) SN Ia models, where the black solid line corresponds to a typical near- M_{Ch} model, and the dotted and dash-dotted lines represent sub- M_{Ch} models with varied core and shell masses.

Jeena et al. (2024), sub-solar values of $[\text{X}/\text{Fe}]$ for α elements result from models with negligible fallback that is particularly relevant for α -poor VMP stars. We thus show a few representative CCSN models without fallback that have $[\text{Mg}/\text{Fe}] \lesssim 0.0$ in Fig. 1b.

2.3 SN Ia Models

In this study, we consider the delayed detonation model for near- M_{Ch} and the double detonation model for sub- M_{Ch} for SN Ia as these are currently considered to be the dominant channels as mentioned in the introduction. In both cases, we adopt the nucleosynthetic yields obtained from high-resolution 3D studies for the explosion of WDs of low metallicity. In near- M_{Ch} models, we adopt the nucleosynthetic yields derived from the delayed detonation model N100_Z0.01 by Seitenzahl et al. (2013a), corresponding to a WD with a central density of $2.9 \times 10^9 \text{ g cm}^{-3}$ and an initial metallicity of $0.01 Z_{\odot}$. For sub- M_{Ch} models, we adopt the yields from eleven double detonation models by Gronow et al. (2021) that have an initial metallicity of $0.001 Z_{\odot}$ with CO core masses ranging from 0.8–1.1 M_{\odot} that have central densities of $\lesssim 2.5 \times 10^9 \text{ g cm}^{-3}$ with He shell masses of 0.02–0.1 M_{\odot} . The sub- M_{Ch} models are labelled with the CO core mass (M_{CO}) and He shell mass (M_{He}), e.g., M09_05 corresponds to a WD with $M_{\text{CO}} = 0.9 M_{\odot}$ and $M_{\text{He}} = 0.05 M_{\odot}$.

Figure 1c shows the abundance pattern of the adopted SN Ia models. In both near- M_{Ch} and sub- M_{Ch} models, there is negligible production of elements lighter than Si. However, the abundance pattern from Si to Fe peak varies significantly among the various sub- M_{Ch} models that are also distinct from the near- M_{Ch} model. In the near- M_{Ch} model, the abundance of α elements is sub-solar ($[\alpha/\text{Fe}] < 0$) for elements up to Ti (see Fig. 1c). The sub- M_{Ch} yield patterns, on the other hand, depend on both M_{CO} and M_{He} . The lowest mass $M_{\text{CO}} \sim 0.8 M_{\odot}$ can even produce α -enhanced ($[\alpha/\text{Fe}] > 0$) abundance pattern from Si–Cr resulting from incomplete Si burning of both the CO core and He shell. With higher $M_{\text{CO}} \gtrsim 1.0 M_{\odot}$ and $M_{\text{He}} \sim 0.1 M_{\odot}$, the α -poor feature, that is usually associated with SN Ia, is seen for elements from Si to Ca although Ti to Cr continues to be enhanced with super-solar values of $[\text{X}/\text{Fe}]$ in some of the models. The enhanced Ti–Cr in such models is exclusively due to the contribution from He shell burning that invariably undergoes incomplete Si burning. The contribution of He shell burning to the final ejecta is particularly high for $M_{\text{CO}} \lesssim 1 M_{\odot}$ with intermediate values of $M_{\text{He}} \sim 0.05 M_{\odot}$. Thus, the combination of sub-solar values of $[\text{X}/\text{Fe}]$ from Si to Ca along with super-solar values from Ti–Cr is a unique feature found only in some of the sub- M_{Ch} models that is otherwise not found in either CCSN or near- M_{Ch} models. Additionally, solar $[\text{Mn}/\text{Fe}] \sim 0$, usually associated with near- M_{Ch} models, is also seen in the lower CO core mass models whereas, for CO core masses of $\gtrsim 1 M_{\odot}$, $[\text{Mn}/\text{Fe}]$ is always sub-solar. Lastly, $[\text{Ni}/\text{Fe}]$ is sub-solar in all sub- M_{Ch} models which is distinct from near- M_{Ch} model that has $[\text{Ni}/\text{Fe}] \sim 0.1$.

In comparison to the CCSN models, the major difference is that SN Ia models have negligible production of elements lighter than Si and mostly have sub-solar values of $[\text{X}/\text{Fe}]$ for α elements from Si to Ca. We note that CCSN models that do not undergo fallback can also have similar features as discussed in Sec. 2.2. However, the unique feature seen in some of the sub- M_{Ch} SN Ia models from Ti to Cr mentioned above is not found in any of the CCSN models. Even after accounting for mixing and fallback, all CCSN models have sub-solar values of $[\text{X}/\text{Fe}]$ for Ti to Cr. This is because elements from Ti to Fe are mostly produced in the same region within the CCSN ejecta and are thus insensitive to the details of mixing and fallback. Similarly, $[\text{Mn}/\text{Fe}] \sim 0$ is not found in any of the CCSN models but is a key

signature of the near- M_{Ch} model. We note that $[\text{Mn}/\text{Fe}] \gtrsim 0$ can also be found in some of the lighter CO core mass sub- M_{Ch} models but the combination sub-solar values of $[\text{X}/\text{Fe}]$ for Mg to Ca along with $[\text{Mn}/\text{Fe}] \sim 0$ is only found in the near- M_{Ch} model.

3 MATCHING THE ABUNDANCE PATTERN OF SDSSJ0018-0939

In order to match the observed abundance pattern of SDSSJ0018-0939, we consider five distinct scenarios for the origin of elements in VMP stars formed in the early Galaxy. In the first case, we assume all elements are exclusively produced by a single PISN. In the second case, we assume all elements are exclusively produced by a single CCSN undergoing mixing and fallback. Next, we consider the mixing of the ejecta from a single CCSN with that of either a near- M_{Ch} or sub- M_{Ch} SN 1a. Finally, we consider the mixing of ejecta of two CCSNe.

3.1 Best-fit models from a single PISN

In order to find the best-fit model, we follow the same procedure as detailed in Jeena et al. (2023). For each element X_i , we define the number yield $Y_{X_i} = \sum_j m(X_i^j)/A_j$, where $m(X_i^j)$ is the yield of the j^{th} isotope and A_j is the corresponding mass number. The ratio of the number abundance N of any element X_i relative to a reference element X_{R} can be written as

$$\frac{N_{X_i}}{N_{X_{\text{R}}}} = \frac{Y_{X_i}}{Y_{X_{\text{R}}}}. \quad (1)$$

Following this, the best-fit model parameters are determined using a χ^2 prescription as discussed in Heger & Woosley (2010) and more recently in Jeena et al. (2023, 2024). In this prescription, χ^2 is defined as the square of the deviation between the observed and predicted values summed over all elements. The square of the inverse of the observed uncertainty (σ_i) is used as the weights for each element where we set $\sigma_i = \max(\sigma_i, 0.1)$ to ensure that χ^2 is not excessively sensitive to elements with extremely low values of σ_i .

3.2 Best-fit models from a single CCSN

The procedure for finding the best-fit model for CCSN is similar to the one for PISN described above. In this case, however, both Y_{X_i} and $Y_{X_{\text{R}}}$ depend on the two free parameters $M_{\text{cut,fin}}$ and f_{cut} . For every CCSN progenitor, we consider all possible combinations of the two parameters to generate thousands of models. The process is then repeated for each CCSN progenitor. The best-fit model is again determined by the χ^2 formulation mentioned above. In order to be consistent with the dilution found in simulations of metal mixing from CCSN, we only consider solutions for which the effective dilution mass from CCSN is greater than $M_{\text{dil,CCSN}}^{\text{min}} = 10^4 M_{\odot}$ for explosion energies of $\leq 1.2 \times 10^{51}$ erg and $M_{\text{dil,CCSN}}^{\text{min}} = 10^5 M_{\odot}$ for 1.2×10^{52} erg. These values correspond roughly to the minimum value of the effective dilution mass for the CCSN ejecta from the detailed simulation of inhomogeneous metal mixing in the early Galaxy (Chiaki et al. 2018; Magg et al. 2020).

We note here that detailed 3D simulations have shown that Sc is dominantly produced by neutrino-processed proton-rich ejecta that are not modelled in our 1D calculations. Sc yield in 3D models, that include detailed neutrino interaction, can be a factor of $\gtrsim 10$ higher than the corresponding 1D model (Sieverding et al. 2020; Wang &

Burrows 2024). Because of this reason, in our analysis, we treat the measured abundance of Sc (if available) as an upper limit.

3.3 Best-fit models from the mixing of CCSN and SN 1a ejecta

In order to determine the best-fit model based on the mixing of ejecta from two distinct sources, we consider the prescription used in the recent work Jeena et al. (2023). In this prescription, the mixing of the ejecta of the two sources, i.e., CCSN and SN 1a, is parameterized by a single parameter α given by

$$\alpha = \frac{M_{\text{dil,CCSN}}}{M_{\text{dil,CCSN}} + M_{\text{dil,1a}}}, \quad (2)$$

where $M_{\text{dil,CCSN}}$ and $M_{\text{dil,1a}}$ are the effective dilution masses from CCSN and SN 1a, respectively. Following the mixing procedure, the number abundance of any element X_i relative to a reference element X_{R} can be written as

$$\frac{N_{X_i}}{N_{X_{\text{R}}}} = \frac{Y_{X_i}}{Y_{X_{\text{R}}}} = \frac{\alpha Y_{X_i,1a} + (1 - \alpha) Y_{X_i,\text{CCSN}}(M_{\text{cut,fin}}, f_{\text{cut}})}{\alpha Y_{X_{\text{R}},1a} + (1 - \alpha) Y_{X_{\text{R}},\text{CCSN}}(M_{\text{cut,fin}}, f_{\text{cut}})}, \quad (3)$$

where the subscript ‘1a’ and ‘CCSN’ are used for the number yields corresponding to SN 1a and CCSN, respectively. In this case, the final abundance pattern depends on the parameter α in addition to $M_{\text{cut,fin}}$ and f_{cut} . The three parameters are then varied to find the best-fit model using the same χ^2 prescription used for PISN and CCSN. For any given fit, the relative contribution from each source to an element X_i , can be quantified by computing the fraction $\eta(X_i)$ of the total elemental yield Y_{X_i} . We compute $\eta(X_i)$ for SN 1a and CCSN, i.e., $\eta_{1a}(X_i)$ and $\eta_{\text{CCSN}}(X_i)$, where $\eta_{1a}(X_i) + \eta_{\text{CCSN}}(X_i) = 1$.

Depending on the type of SN 1a, we consider two different mixing scenarios:

- CCSN+near- M_{Ch} : we consider mixing of CCSN ejecta with the ejecta from the near- M_{Ch} model from Seitzzahl et al. (2013a).
- CCSN+sub- M_{Ch} : we consider mixing of CCSN ejecta with the ejecta from sub- M_{Ch} models from Gronow et al. (2021) for the various CO core and He shell masses as discussed in Sec. 2.3.

In both cases, we consider mixing and fallback of CCSN models as discussed in Sec. 2.2. Thus, CCSN+near- M_{Ch} and CCSN+sub- M_{Ch} include the mixing between all the combinations of CCSN ejecta from mixing and fallback with SN 1a ejecta. The mixing parameter α controls the mixing of the CCSN and SN 1a ejecta, where the values are varied from a lowest value of 10^{-5} (negligible SN 1a contribution) to a maximum value of 1 (exclusively SN 1a contribution). In both scenarios, we find the best-fit models by minimising χ^2 as mentioned earlier, where we again impose the criteria that both $M_{\text{dil,1a}}$ and $M_{\text{dil,CCSN}}$ are greater than a minimum dilution, where we adopt $M_{\text{dil,1a}}^{\text{min}} = 10^4 M_{\odot}$ and the same values of $M_{\text{dil,CCSN}}^{\text{min}}$ as mentioned in Sec. 3.2.

3.4 Best-fit models from the mixing of ejecta from two CCSNe

It is important to note that in the scenarios involving the mixing of ejecta between CCSN and SN 1a discussed above, the best-fit χ^2 is guaranteed to be less than the value from a single CCSN. This is because the case of pure CCSN ejecta with no SN 1a contribution is also included among the range of the possibilities of CCSN+SN 1a corresponding to $\alpha \approx 0$. Thus, in order to evaluate whether an observed abundance pattern can be fit better by CCSN relative to CCSN+SN 1a, we consider the possibility of mixing the ejecta from two different CCSN. Unfortunately, each CCSN progenitor has thousands of possible ejecta corresponding to the different combinations

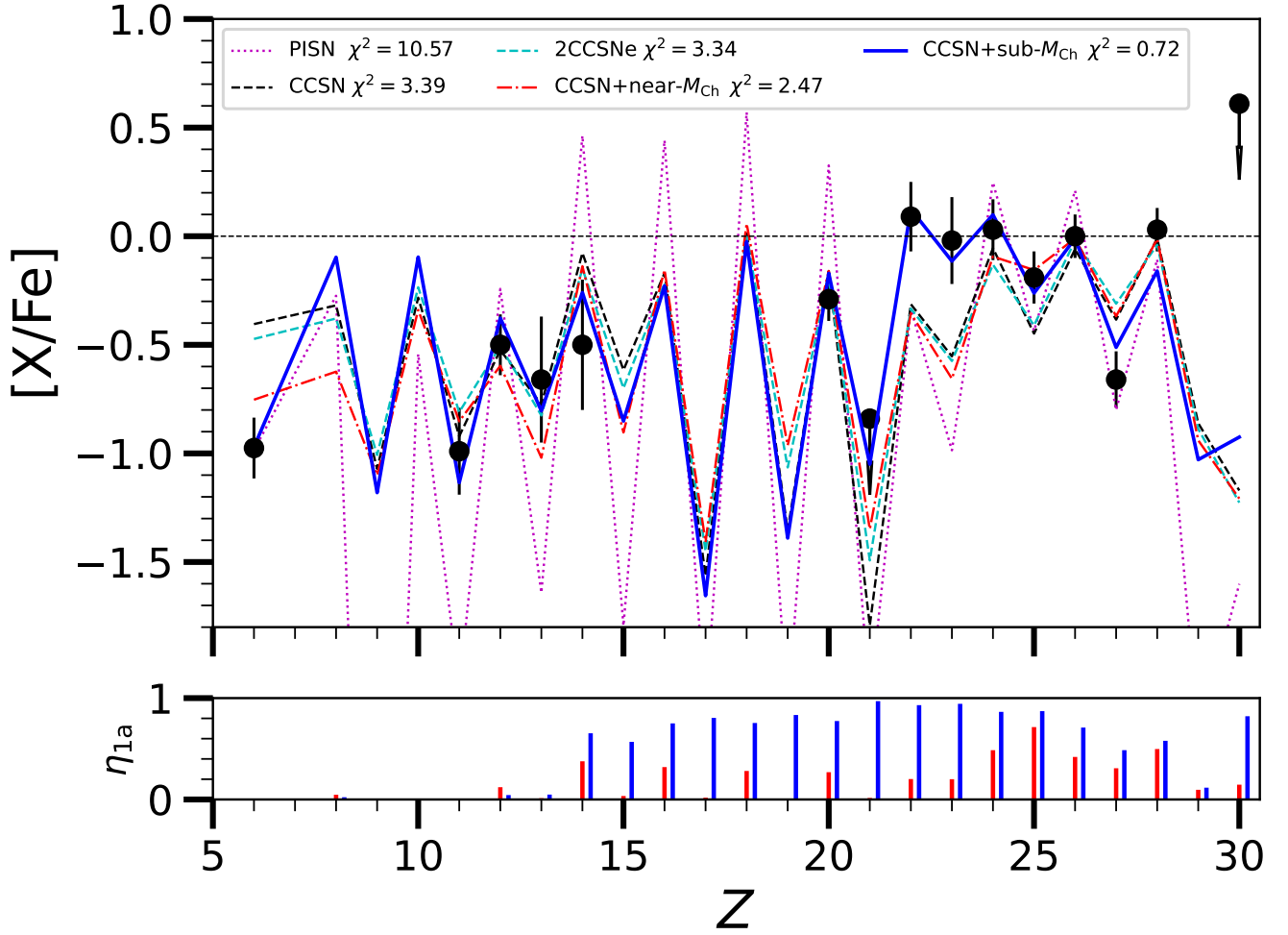


Figure 2. The elemental abundance pattern of SDSSJ0018-0939 compared with the best-fit models from various scenarios: PISN (magenta dotted line), CCSN (black dashed line), 2CCSNe (cyan dashed line), CCSN+near- M_{Ch} (red dash-dotted line) and CCSN+sub- M_{Ch} (blue solid line). The red and blue vertical solid lines in the bottom panel show the fraction of elements η_{1a} produced by near- M_{Ch} and sub- M_{Ch} SN Ia models, respectively.

of $M_{\text{cut,fin}}$ and f_{cut} . This makes the total number of ejecta models, from all combinations of parameters for combining the ejecta from two CCSN, exceedingly large ($\geq 10^{11}$ models) and computationally prohibitively expensive. We thus explore the limited parameter space of combining the ejecta from mixing and fallback from a CCSN with that of another CCSN that undergoes no fallback, i.e., $f_{\text{cut}} = 1$. Although this explores a tiny fraction of the total parameter space of the mixing between two CCSN, the combinations cover the most important part relevant for α -poor VMP stars that tend to prefer CCSN models with negligible fallback as fallback invariably increases $[\alpha/\text{Fe}]$. For brevity, we refer to this scenario as 2CCSNe from hereon. In order to find the best-fit model, we follow the same procedure as used for the mixing between CCSN and SN Ia as discussed in Sec. 3.3 where SN Ia is replaced by the second CCSN ejecta with no fallback.

4 BEST-FIT MODELS FOR SDSSJ0018-0939

Figure 2 shows the best-fit models from all possible combinations, i.e., exclusively from a PISN (magenta dotted line), a single

CCSN (black dashed line), 2CCSNe (cyan dashed line), CCSN+near- M_{Ch} SN Ia (red dash-dotted line), and CCSN+sub- M_{Ch} SN Ia (blue solid line). The fraction of elements produced by SN Ia, i.e., η_{1a} , from the two SN Ia mixing scenarios, is also shown in the bottom panel of Fig. 2. The best-fit models and the corresponding parameters are listed in Table 1.

As can be seen from Fig. 2, the best-fit PISN model provides a very poor fit with $\chi^2 = 10.57$ and fails to fit multiple elements with particularly large deviation from the observed values for Na, Al, Si, Ca, Ti and V. Compared to PISN models, the best-fit CCSN model provides a better fit with $\chi^2 = 3.39$, and can fit most of the elements from Na to Ca and Cr to Ni. However, even after accounting for the 1σ uncertainty, it fails to fit the observed abundances of several elements such as C, Si, Ti, V, Mn, and Co with large deviations of ~ 0.5 dex from the observed values for C, Ti, and V. The situation does not improve when mixing from 2CCSNe is considered with a negligible improvement in the quality of fit with a $\chi^2 = 3.34$. The particularly poor fit for C, Ti, and V for the best-fit models from both single CCSN and 2CCSNe scenarios strongly indicates that the observed pattern cannot be explained by CCSN ejecta alone. Here, it is important to note that because of the high value of $\log g = 5$, the

Table 1. Best-fit models and parameters along with the dilution mass for SDSSJ0018-0939.

Model	Model name	E_{exp} ($\times 10^{51}$ erg)	χ^2	α	ΔM_{cut} (M_{\odot})	ΔM_{fb} (M_{\odot})	$M_{\text{dil,CCSN}}$ ($\times 10^4 M_{\odot}$)	$M_{\text{dil,1a}}$ ($\times 10^4 M_{\odot}$)
PISN	120 M_{\odot} He core	71.0	10.57	–	–	–	4.0×10^4	–
CCSN	z12.1- Y_e	1.2	3.39	–	0.11	0.08	1.98	–
2CCSNe	z11.3- Y_e +	1.2	3.34	0.33	0.00	0.00	2.87	–
	z11.9- Y_e				0.11	0.06	5.82	–
CCSN+near- M_{Ch}	z11.3- Y_e +	1.2	2.47	0.11	0.88	0.008	2.98	39.50
	N100_Z0.01							
CCSN+sub- M_{Ch}	z30- Y_e +	1.2	0.72	0.57	4.23	1.60	24.60	18.50
	M10_05							

highly sub-solar value of $[C/Fe] \sim -1$ cannot be attributed to the destruction of C due to internal mixing in SDSSJ0018-0939. Thus, the very low $[C/Fe]$ in this star is inherited from the birth material and a strong indicator of additional Fe contribution from SN 1a. This can be seen clearly from the best-fit CCSN+near- M_{Ch} model that provides a slightly better fit with a lower $\chi^2 = 2.47$ which is largely due to a much better fit to C. Compared to CCSN models, higher $[Mn/Fe]$ from near- M_{Ch} models leads to a perfect fit for Mn, but is counterbalanced by a worse fit to Al. Similar to the best-fit CCSN models, the best-fit CCSN+near- M_{Ch} model cannot fit C, Ti, V, and Co, with a particularly large deviation from the observed values for Ti and V.

In contrast, the best-fit model from the CCSN+sub- M_{Ch} , resulting from the mixing of the ejecta from a $30 M_{\odot}$ CCSN and a sub- M_{Ch} SN 1a with $M_{\text{CO}} = 1 M_{\odot}$ and $M_{\text{He}} = 0.05 M_{\odot}$, provides an excellent fit to the observed abundance pattern with the lowest $\chi^2 = 0.72$. In particular, the best-fit CCSN+sub- M_{Ch} model can explain almost all the elements except for Ni and can perfectly fit C along with all elements from Ti–Fe. Importantly, the near perfect fit for Ti to Cr is entirely due to the contribution for sub- M_{Ch} SN 1a as is evident from the fact that $\eta_{1a} \sim 1$ (see the bottom panel of Fig. 2) from Sc to Mn for the best-fit model. We note that the particular feature of $[X/Fe] \geq 0$ for Ti, V, and Cr with $[Ti/Cr] \geq 0$ can only be fit by sub- M_{Ch} models that arise from the incomplete Si burning of the He shell as discussed earlier in Sec. 2.3. Ejecta from sub- M_{Ch} SN 1a also contributes majorly to all elements from Si–Ca as well as Fe–Ni with $\eta_{1a} \geq 0.5$. The CCSN ejecta, on the other hand, accounts for almost all the elements lighter than Si but is a subdominant contributor to elements from S–Fe. For elements such as Si, Co, and Ni, both CCSN and sub- M_{Ch} ejecta make comparable contributions. Because the contribution from CCSN ejecta to the Fe group is non-negligible, this forces the CCSN model to have a very low fallback of the innermost material containing Fe group elements in order to fit the sub-solar values of $[X/Fe]$ from C to Si.

It is important to note that in the CCSN+sub- M_{Ch} scenario, although the contribution of both CCSN and sub- M_{Ch} SN 1a is required to fit the full observed abundance pattern, the primary reason for the excellent fit is driven by the crucial contribution of sub- M_{Ch} SN 1a that can fit the unique pattern from Ti–Cr. We find that in addition to the $30 M_{\odot}$ CCSN model that provides the best fit, many other CCSN models that have a low fallback give comparable fits with very low $\chi^2 \lesssim 0.8$ when their ejecta is mixed with the sub- M_{Ch} SN 1a model. Similar to the best-fit CCSN+sub- M_{Ch} model, all such models have $\eta_{1a} \geq 1$ for elements from Ti–Cr, confirming the fact that the primary reason for the excellent fit is due to sub- M_{Ch} SN 1a contribution.

5 SIGNATURE OF SN 1A IN OTHER STARS?

As mentioned in the introduction, although α -poor VMP stars have been associated with SN 1a, very few studies have attempted to identify the observed pattern in individual stars with theoretical yields from SN 1a. An exception to this has been the work by McWilliam et al. (2018) where conclusive evidence of sub- M_{Ch} SN 1a origin for the star COS171 in Ursa Minor was reported. However, they only considered the contribution from SN 1a and neglected any contribution from CCSN. Recently, Reggiani et al. (2023) has also identified three α -poor stars that show possible signatures of sub- M_{Ch} SN 1a contribution. Among the three, BD+80245 has the highest metallicity of $[Fe/H] = -1.73$ whereas SMSS J034249–284216 and HE 0533–5340 have metallicities of $[Fe/H] = -1.97$ and -2.44 , respectively. Similar to McWilliam et al. (2018), this study also neglected the contribution from CCSN. Below we analyse these stars for the different scenarios considered for SDSSJ0018-0939 to see if the observed abundance patterns can be explained by PISN or CCSN, or whether SN 1a contribution from either near- M_{Ch} or sub- M_{Ch} models is required.

5.1 COS171

COS171 is an α -poor star with $[Fe/H] = -1.35$ which happens to be one of the highest metallicity stars in Ursa Minor (Cohen & Huang 2010). Because this star has a low $\log g = 0.8$, the initial C in the star would have been considerably depleted (Placco et al. 2014). For this reason, we treat the observed value of C in this star as a lower limit. We analysed this star for all the possible scenarios and the best-fit models are shown in Fig. 3a and the corresponding details are listed in Table 2.

The best-fit PISN model provides an extremely poor fit with $\chi^2 = 35$ and clearly cannot explain the abundance pattern. For a single CCSN, the best-fit model has a $\chi^2 = 4.59$ and can fit all elements from Na to Ca and V to Mn. However, the quality of fit is particularly poor for Ti and all elements from Fe to Cu as the fit is well beyond the observed 1σ uncertainty. Additionally, it fails to fit O and Zn. The best-fit model from 2CCSNe provides a slightly better fit with a $\chi^2 = 4.03$ with somewhat better fits for O and Zn. However, similar to the single CCSN best-fit model, it gives a poor fit for Ti and all elements from Fe to Cu. The quality of fit remains unchanged for the best-fit CCSN+near- M_{Ch} model as the best-fit corresponds to the combination where there is negligible contribution from SN 1a as is evident from η_{1a} from Fig. 3a. Lastly, for the best-fit CCSN+sub- M_{Ch} model, the quality is marginally better than the best-fit 2CCSNe model with a $\chi^2 = 3.09$. This model can additionally fit O, Cu, and

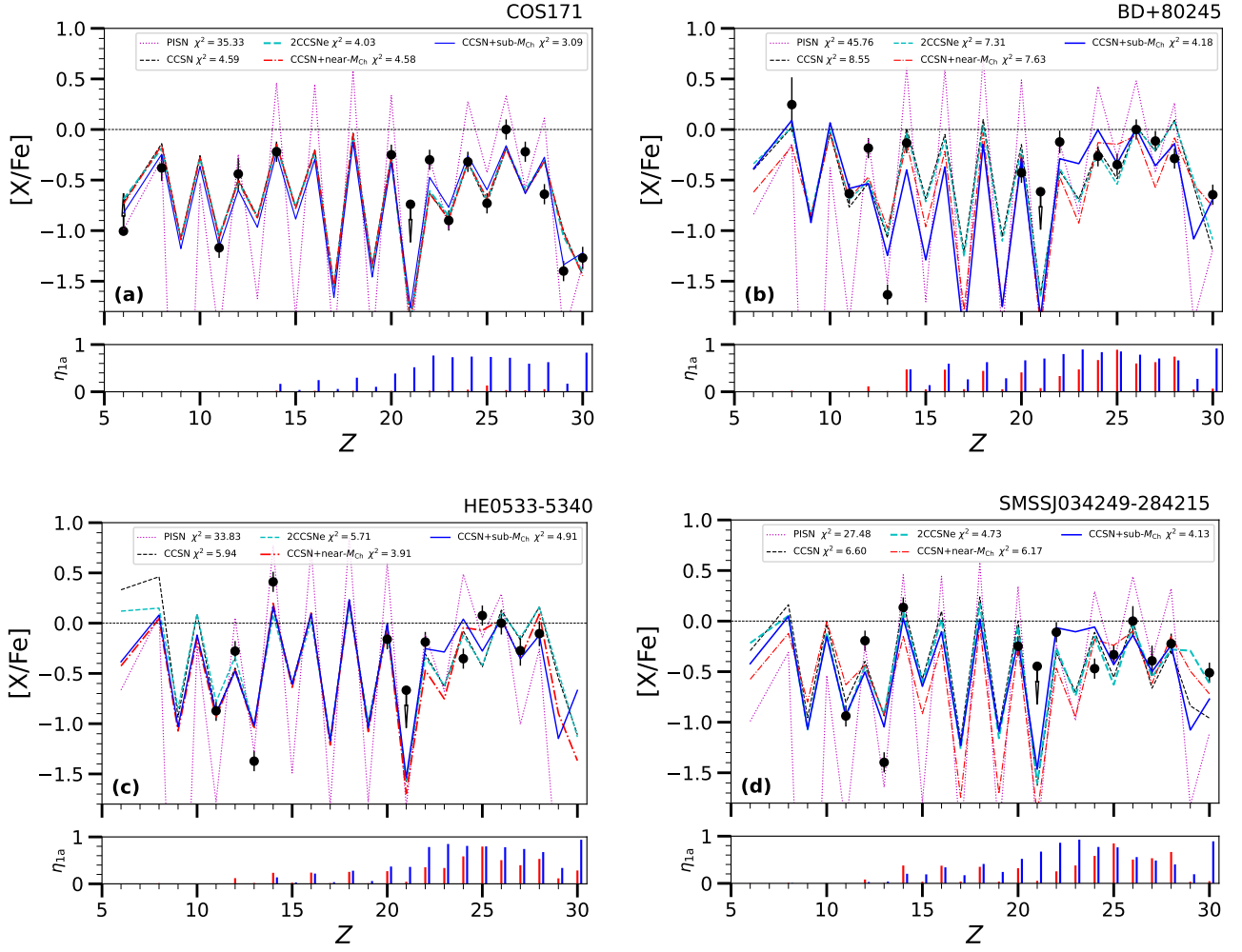


Figure 3. Same as Fig. 2, but for stars COS171, BD+80245, HE0533–5340, and SMSSJ034249–284216.

Zn along with a slightly better fit for Ti at the cost of a poorer fit for V and Mn.

Surprisingly, the primary reason for the slightly better fit for the best-fit CCSN+sub- M_{Ch} model is that it can perfectly fit Cu even though SN Ia contribution to Cu is negligible with $\eta_{Ia} \sim 0.2$ (see the bottom panel in Fig. 3a).

We note here that COS171 is not a VMP star. Thus, if the origin of elements in COS171 is entirely from CCSN, it is likely to have come from ejecta from several events. However, as mentioned earlier, combining ejecta from multiple sources is not possible as it is computationally expensive. Thus, in order to test whether multiple CCSN ejecta can match the observed abundance pattern we lower the $M_{dil,CCSN}^{min}$ to $5 \times 10^3 M_{\odot}$ for a single CCSN so that it can match the overall high metallicity in addition to the relative abundance pattern. Interestingly, we find that even with a lower value of minimum dilution, the best-fit model for a single CCSN remains unchanged with a $M_{dil,CCSN} = 1.1 \times 10^4 M_{\odot}$ and a $\chi^2 = 4.59$. The best-fit model for 2CCSNe does slightly better and can additionally fit O and Zn but continues to give a poor fit for Ti and elements from Fe to Cu. The corresponding value of $\chi^2 = 3.36$ is comparable to the best-fit CCSN+sub- M_{Ch} model. The reason for the overall poor fit is primarily due to the peculiar abundance pattern from Fe to Zn. In

particular, highly sub-solar $[Ni/Fe] \sim -0.7$ along with super-solar $[Co/Ni] \sim 0.5$ cannot be produced by either CCSN or SN Ia.

In summary, even though the best-fit CCSN+sub- M_{Ch} model provides the overall best fit with the lowest χ^2 , the quality of fit is comparable to the best-fit 2CCSNe model while the overall quality of fit is poor for both. Thus, the observed abundance pattern in COS171 cannot be strongly attributed to SN Ia in sharp contrast to SDSSJ0018-0939.

5.2 BD+80245

The best-fit for BD+80245 for the different scenarios is shown in Fig. 3b with the corresponding details listed in Table 2. Similar to COS171, PISN provides an extremely poor fit with $\chi^2 = 45.76$. The quality of fit for a single CCSN and 2CCSNe are comparable with best-fit χ^2 of 8.55 and 7.31, respectively, with an overall poor fit as they cannot match the abundance of multiple elements with particularly large deviation from the observed abundances for Mg, Al, Ti, Ni, and Zn. The quality of fit is similar for the best-fit CCSN+near- M_{Ch} model with a $\chi^2 = 7.63$. The best-fit CCSN+sub- M_{Ch} model does give the lowest $\chi^2 = 4.18$ even though the overall quality of fit is only slightly better. While it does provide a better fit for Ti, Ni

Table 2. Same as Table. 1, but for stars COS171, BD+80245, HE0533-5340, and SMSSJ03429-284216.

Star	Model	Model name	E_{exp} ($\times 10^{51}$ erg)	χ^2	α	ΔM_{cut} (M_{\odot})	ΔM_{fb} (M_{\odot})	$M_{\text{dil,CCSN}}$ ($\times 10^4 M_{\odot}$)	$M_{\text{dil,SN 1a}}$ ($\times 10^4 M_{\odot}$)
COS171	PISN	125 M_{\odot} He core	78.8	35.30	–	–	–	3.2×10^3	–
	CCSN	z23- Y_e	1.2	4.59	–	0.11	0.11	1.10	–
	2CCSNe	z11.7- Y_e +	1.2	4.03	0.57	0.00	0.00	1.36	–
		z23- Y_e	1.2	–	–	0.21	0.20	1.02	–
	2CCSNe ($M_{\text{dil,CCSN}}^{\text{min}} = 5 \times 10^3 M_{\odot}$)	z11.5- Y_e +	1.2	3.36	0.50	0.00	0.00	0.50	–
		z14.1- Y_e	1.2	–	–	0.20	0.19	0.50	–
	CCSN+near- M_{Ch}	z23- Y_e +	1.2	4.58	0.02	0.11	0.11	1.14	55.70
	CCSN+sub- M_{Ch}	N100_Z0.01 z23- Y_e +	1.2	3.09	0.32	0.68	0.47	1.41	2.99
BD+80245	PISN	125 M_{\odot} He core	78.8	45.7	–	–	–	4.3×10^3	–
	CCSN	z20.5- Y_e	1.2	8.55	–	1.45	0.29	1.00	–
	2CCSNe ($M_{\text{dil,CCSN}}^{\text{min}} = 5 \times 10^3 M_{\odot}$)	z20.5- Y_e	1.2	8.37	–	2.11	1.28	0.51	–
		z10.1- Y_e +	1.2	7.31	0.50	0.00	0.00	1.00	–
	2CCSNe ($M_{\text{dil,CCSN}}^{\text{min}} = 5 \times 10^3 M_{\odot}$)	z20.5- Y_e	1.2	–	–	1.45	0.51	1.00	–
		z10.1- Y_e +	1.2	6.58	0.50	0.00	0.00	0.51	–
	CCSN+near- M_{Ch}	z20.5- Y_e	1.2	–	–	2.21	1.63	0.51	–
	CCSN+sub- M_{Ch}	z17.2- S_4 +	1.2	7.63	0.19	1.26	0.03	1.09	4.64
HE0533-5340	PISN	110 M_{\odot} He core	56.4	33.83	–	–	–	1.7×10^4	–
	CCSN	z22- Y_e	1.2	5.94	–	3.08	2.68	1.05	–
	2CCSNe	z20.5- Y_e +	1.2	5.71	0.13	0.00	0.00	1.07	–
		z13.2- Y_e	1.2	–	–	0.60	0.59	7.16	–
	CCSN+near- M_{Ch}	z22- Y_e	1.2	3.91	0.23	0.68	0.40	8.54	28.60
		N100_Z0.01	1.2	–	–	–	–	–	–
	CCSN+sub- M_{Ch}	z22- Y_e	1.2	4.91	0.28	0.68	0.58	7.77	20.00
	M09_03	1.2	–	–	–	–	–	–	
SMSSJ034249-284216	PISN	130 M_{\odot} He core	87.3	27.48	–	–	–	1.3×10^4	–
	CCSN	z22- S_4	1.2	6.60	–	1.74	0.00	2.00	–
	2CCSNe	z22- S_4 +	1.2	4.73	0.24	0.00	0.00	1.01	–
		z12.7- S_4	1.2	–	–	0.40	0.18	3.19	–
	CCSN+near- M_{Ch}	z17.2- S_4 +	1.2	6.17	0.14	0.88	0.00	2.10	12.80
	CCSN+sub- M_{Ch}	N100_Z0.01 z22- Y_e	1.2	4.13	0.23	0.88	0.66	2.70	9.10
M10_10	1.2	–	–	–	–	–	–		

and Zn, the fit is quite poor for Mg, Al, Si, Cr, and Co with large deviations from the observed values well beyond the 1σ uncertainty.

Because BD+80245 has a metallicity of $[\text{Fe}/\text{H}] = -1.73$, we also considered the possibility of reducing $M_{\text{dil,CCSN}}^{\text{min}} = 5 \times 10^3 M_{\odot}$ similar to COS171. In this case, the quality of fit for the best-fit model from a single CCSN remains almost unchanged with $\chi^2 = 8.37$, the value is slightly better for the best-fit model from 2CCSNe with $\chi^2 = 6.58$. Despite the lower χ^2 , the quality of fit remains poor as these models cannot match the abundance of any additional elements. The reason for the overall poor fit is primarily due to Al and Mg which are produced exclusively by CCSN. In particular, it has an extremely sub-solar value of $[\text{Al}/\text{Fe}] \sim -1.7$ leading to highly super-solar $[\text{Mg}/\text{Al}] \sim 1.2$. This cannot be matched by any of the CCSN models which leads to an overall poor fit for all models. We note that the best-fit PISN model can match the low Al along with the highly super-solar $[\text{Mg}/\text{Al}]$ but gives an extremely poor fit for almost all other elements.

Thus, similar to COS171, among all the scenarios, although CCSN+sub- M_{Ch} provides the best fit, the quality of fit is poor and it is difficult to claim a clear signature for SN 1a contribution for BD+80245 in contrast to SDSSJ0018-0939.

5.3 HE0533-5340

The best-fit models for HE0533-5340 are shown in Fig. 3c and the details of the models and best-fit parameters are listed in Table 2. Similar to other stars, the best-fit PISN model provides an extremely poor fit with a $\chi^2 = 33.8$. Unlike COS171 and BD+80245, the best-fit model from the CCSN+near- M_{Ch} provides the best overall fit with $\chi^2 = 3.9$. The primary reason for CCSN+near- M_{Ch} being the best fit is the elevated $[\text{Mn}/\text{Fe}] \sim 0.1$ which is a key signature of the near- M_{Ch} model. The overall quality of fit, however, is poor as the best-fit model cannot match multiple elements such as Mg, Al, Si, Ti, Cr, and Ni. The best-fit model from CCSN+sub- M_{Ch} provides a comparable quality of fit with $\chi^2 = 4.91$. Interestingly, although the χ^2 is slightly higher for the best-fit CCSN+sub- M_{Ch} model, it can match more elements such as Ti and Ni within the observed 1σ uncertainty compared to the best-fit CCSN+near- M_{Ch} model. The quality of fit from other scenarios is slightly worse for a single CCSN and 2CCSNe with χ^2 of 5.94 and 5.71, respectively, for the best-fit models. However, compared to CCSN+near- M_{Ch} model, the best-fit 2CCSNe model can fit more elements such as Mg within the 1σ uncertainty. The higher χ^2 in CCSN models is primarily due to their inherent sub-solar $[\text{Mn}/\text{Fe}]$ values that lead to a poor fit to the observed $[\text{Mn}/\text{Fe}] \sim 0.1$. The overall poor quality of fit for the

observed pattern in HE0533-5340 across all scenarios is primarily due to the peculiar abundance features from Mg–Si and Cr–Mn. In particular, similar to BD+80245, the highly sub-solar value of $[\text{Al}/\text{Fe}] \sim -1.4$ with super-solar $[\text{Mg}/\text{Al}] \sim 1.1$ cannot be fit by any CCSN model. Additionally, high super-solar $[\text{Si}/\text{Fe}] \sim 0.5$ cannot be simultaneously fit with extreme sub-solar $[\text{Al}/\text{Fe}]$. Lastly, sub-solar $[\text{Cr}/\text{Mn}]$ cannot be produced by either CCSN or SN 1a leading to a poor fit for Cr for all models.

In summary, even though CCSN+near- M_{Ch} provides the best fit, the overall quality of fit remains poor. Additionally, the quality of fit from other scenarios including 2CCSNe is comparable and can even match more elements within the observed 1σ uncertainty. Consequently, the observed abundance pattern in HE0533-5340 cannot strongly be attributed to SN 1a.

5.4 SMSSJ034249-284216

The best-fit model for SMSSJ034249-284216 from all the scenarios is shown in Fig. 3d. The situation is very similar to COS171, with the best-fit CCSN+sub- M_{Ch} model providing the overall best fit with $\chi^2 = 4.13$ and a comparable quality of fit from the best-fit 2CCSNe model with $\chi^2 = 4.73$. Among these two models, the best-fit CCSN+sub- M_{Ch} model can match the abundance of Ca, Ti, and Mn whereas the best-fit 2CCSNe model can match Si and Zn and vice-versa. Compared to the best-fit CCSN+sub- M_{Ch} model, the best-fit models from a single CCSN and CCSN+near- M_{Ch} provide a slightly worse fit whereas PISN provides an extremely poor fit. The overall quality of fit from all scenarios is poor which is primarily because they completely fail to match the abundances of Mg, Al and Cr. Similar to BD+80245, this star has an extremely sub-solar value of $[\text{Al}/\text{Fe}] \sim -1.4$ leading to highly super-solar $[\text{Mg}/\text{Al}] \sim 1.2$ that cannot be matched by any of the CCSN models. Similar to HE0533-5340, sub-solar $[\text{Cr}/\text{Mn}]$ cannot be produced by any source yielding a poor fit for Cr for all models.

Thus, the situation is similar to COS171 where although the best-fit CCSN+sub- M_{Ch} model provides the overall best fit with the lowest χ^2 , the quality of fit is comparable to the best-fit 2CCSNe model while the overall quality of fit is poor for both. Thus, the observed abundance pattern in SMSSJ034249-284216 cannot be strongly attributed to SN 1a.

5.5 Best-fit without Al for BD+80245, HE0533-5340, and SMSSJ034249-284216

As discussed in the above analysis, the extremely sub-solar value of $[\text{Al}/\text{Fe}]$ is common to all three stars and is one of the primary reasons for the overall poor fit. We note, however, that a substantially higher abundance of $[\text{Al}/\text{Fe}]$ has been reported for both BD+80245 (Ivans et al. 2003) and HE0533-5340 (Cohen et al. 2013) with $\Delta[\text{Al}/\text{Fe}]$ of +0.41 and +0.68 compared to Reggiani et al. (2023). Additionally, Marino et al. (2019) has found similar values of $[\text{Al}/\text{Fe}]$, they have reported extremely high σ of 0.49 for SMSSJ034249-284216. The large variation in Al abundance is likely caused by the fact that the abundance is estimated from only a single line. Because the Al abundance is potentially uncertain and given that it has a large effect on the quality of fit, we repeat the analysis for the three stars by neglecting Al. The best-fit results are presented in Fig. 4. Overall, neglecting Al does lead to a substantial improvement in the quality for all stars. As before, the overall best-fit model for BD+80245 and HE0533-5340 comes from CCSN+sub- M_{Ch} and CCSN+near- M_{Ch} , respectively, with much improved χ^2 of 1.75 and 2.78, respectively.

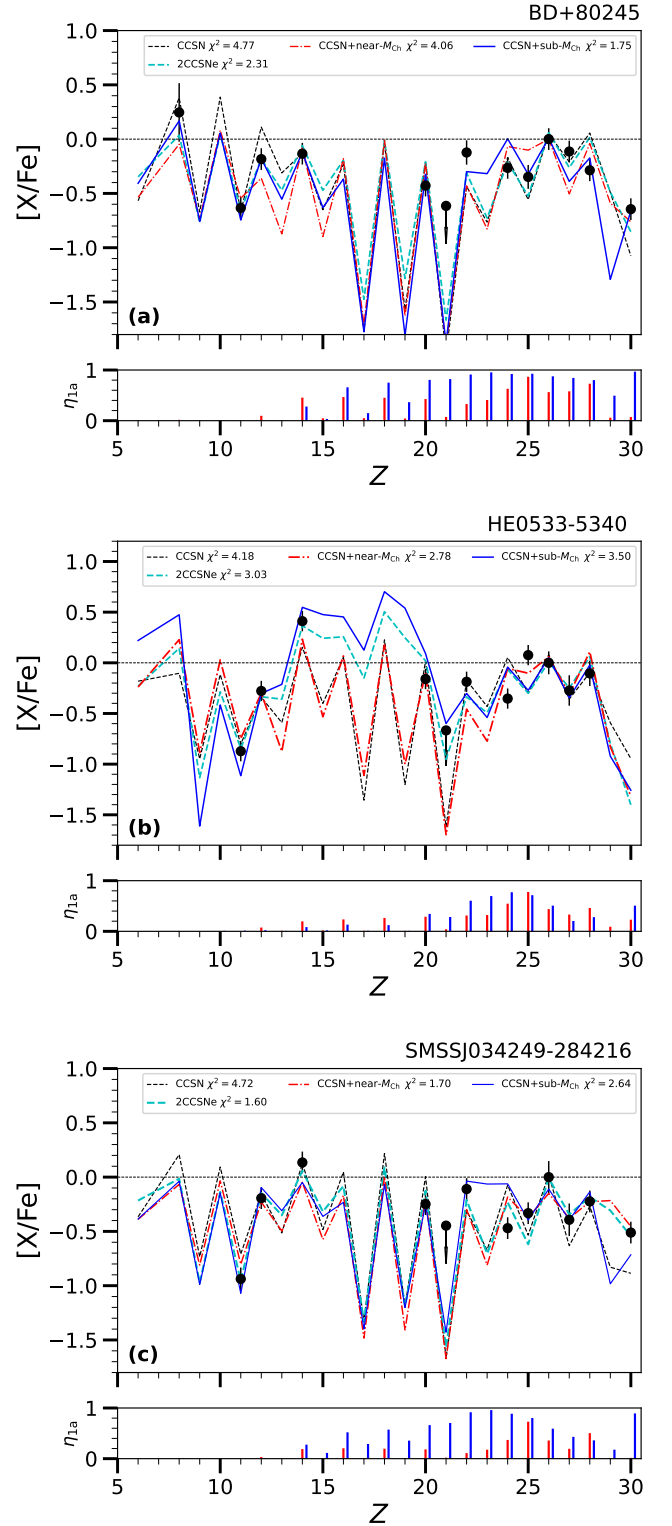


Figure 4. Same as Fig. 3, but Al is neglected.

However, in both cases, the quality of fit from the best-fit 2CC-SNe model is comparable with χ^2 of 2.31 and 3.03 for BD+80245 and HE0533-5340, respectively. Interestingly, for SMSSJ034249-284216, the overall best-fit model is from 2CCSNe with a χ^2 of 1.6 which is closely followed by CCSN+near- M_{Ch} with χ^2 of 1.7.

Thus, in summary, the results clearly show that the abundance pattern in BD+80245, HE0533-5340, and SMSSJ034249-284216 cannot be strongly associated with SN 1a as ejecta from CCSNe alone can also provide comparable fit.

6 SUMMARY AND CONCLUSIONS

SDSSJ0018-0939 is an α -poor VMP star that was previously identified as a star with a possible signature from PISN by Aoki et al. (2014). However, we find that none of the theoretical PISNe abundance patterns is remotely compatible with the observed pattern as the best-fit PISN pattern gives an extremely poor fit with a high χ^2 . Instead, the peculiar abundance pattern observed in SDSSJ0018-0939 can be fit perfectly by the mixing of the ejecta between a $30 M_{\odot}$ CCSN with negligible fallback and a sub- M_{Ch} SN 1a resulting from He detonation of a WD with $M_{\text{CO}} = 1 M_{\odot}$ and $M_{\text{He}} = 0.05 M_{\odot}$. In particular, we find that the unique pattern around the Ti-Cr region with $[X/\text{Fe}] \geq 0$ for Ti, V, and Cr along with $[\text{Ti}/\text{Cr}] \geq 0$ is the key signature of sub- M_{Ch} SN 1a resulting from contribution from He shell burning that is distinct from any other source such as CCSNe or a combination of CCSN and near- M_{Ch} SN 1a. This, in combination with very low $[\text{C}/\text{Fe}] \sim -1$ along with highly sub-solar values of $[X/\text{Fe}]$ for Mg, Si, and Ca, point to a near smoking-gun signature of a star formed from a gas strongly polluted by a sub- M_{Ch} SN 1a.

A clear signature of a sub- M_{Ch} SN 1a in the early Galaxy is particularly interesting as it is consistent with the findings from recent studies that analyzed the observed evolution of $[\text{Mn}/\text{Fe}]$ and $[\text{Ni}/\text{Fe}]$ in the Milky Way and dwarf galaxies (Seitenzahl et al. 2013b; Kobayashi et al. 2020; Eitner et al. 2020, 2023). These studies conclude that the contribution of sub- M_{Ch} SN 1a is crucial and could account for up to ~ 50 – 75% of the total SN 1a. Furthermore, there are indications that sub- M_{Ch} SN 1a is dominant in the early times in dwarf galaxies whereas near- M_{Ch} SN 1a becomes important at later times (Kirby et al. 2019; de los Reyes et al. 2020). Thus, it is not surprising that a signature from a sub- M_{Ch} SN 1a is more likely to be found in VMP stars.

We also analyzed four stars, namely, COS171, BD+80245, HE0533-5340, and SMSSJ034249-284216, that have been identified previously as ones that show a possible signature of SN 1a contribution (McWilliam et al. 2018; Reggiani et al. 2023). In contrast to earlier analysis, we find that the mixing of ejecta from CCSNe can provide fits to all of these stars that are comparable to the fit obtained from models considering the mixing of CCSN and SN 1a. Thus, unlike SDSSJ0018-0939, the abundance pattern observed in these stars cannot be unambiguously attributed to SN 1a.

It is important to note that the significance of SDSSJ0018-0939 as the star with the clearest signature of SN 1a among all VMP stars is ultimately based on the robustness of observed abundances of key elements such as C, Ti, V, and Cr. In this regard, we note that large discrepancies in the estimated abundances of elements is sometimes found when a given star is analyzed by different groups. Large changes in the abundance of key elements can consequently affect and even change their association with a particular source.. A recent example of this is the chemically peculiar star LAMOST J1010+2358 that was first reported by Xing et al. (2023) whose estimated abundance pattern is found to be considerably different in

subsequent analysis by Skúladóttir et al. (2024) and Thibodeaux et al. (2024). Thus, it is important that SDSSJ0018-0939 is also analyzed by independent groups to confirm whether the observed abundance pattern is robust.

Our results highlight the importance of α -poor VMP stars as powerful probes for gaining crucial insights about SN 1a. Such stars provide the only direct probe for detailed nucleosynthesis in SN 1a that can differentiate between near- M_{Ch} and sub- M_{Ch} models. However, we also find that not all α -poor VMP stars require SN 1a contribution as some of the CCSN models that do not undergo substantial fallback can also match the observed abundance pattern equally well. Thus, a clear association of SN 1a with such stars should only be made after careful analysis. Notwithstanding this, future detections of more α -poor VMP stars with detailed abundance patterns from multiple elements are required to find more stars such as SDSSJ0018-0939 that can be used to gain crucial insights into SN 1a and their contribution to the early Galaxy.

DATA AVAILABILITY

Data is available upon reasonable request.

REFERENCES

- Aoki W., Tominaga N., Beers T. C., Honda S., Lee Y. S., 2014, *Science*, **345**, 912
- Beers T. C., Christlieb N., 2005, *ARA&A*, **43**, 531
- Bravo E., 2019, *A&A*, **624**, A139
- Bravo E., Badenes C., Martínez-Rodríguez H., 2019, *MNRAS*, **482**, 4346
- Cayrel R., et al., 2004, *A&A*, **416**, 1117
- Chiaki G., Susa H., Hirano S., 2018, *MNRAS*, **475**, 4378
- Cohen J. G., Huang W., 2010, *ApJ*, **719**, 931
- Cohen J. G., Christlieb N., Thompson I., McWilliam A., Shectman S., Reimers D., Wisotzki L., Kirby E., 2013, *ApJ*, **778**, 56
- Cybur R. H., Fields B. D., Olive K. A., 2002, *Astroparticle Physics*, **17**, 87
- Eitner P., Bergemann M., Hansen C. J., Cescutti G., Seitenzahl I. R., Larsen S., Plez B., 2020, *A&A*, **635**, A38
- Eitner P., Bergemann M., Ruiter A. J., Avril O., Seitenzahl I. R., Gent M. R., Côté B., 2023, *A&A*, **677**, A151
- Fink M., et al., 2014, *MNRAS*, **438**, 1762
- Frebel A., Norris J. E., 2015, *ARA&A*, **53**, 631
- Gronow S., Côté B., Lach F., Seitenzahl I. R., Collins C. E., Sim S. A., Röpke F. K., 2021, *A&A*, **656**, A94
- Heger A., Woosley S. E., 2002, *ApJ*, **567**, 532
- Heger A., Woosley S. E., 2010, *ApJ*, **724**, 341
- Ishigaki M. N., Tominaga N., Kobayashi C., Nomoto K., 2014, *ApJ*, **792**, L32
- Ivans I. I., Sneden C., James C. R., Preston G. W., Fulbright J. P., Höflich P. A., Carney B. W., Wheeler J. C., 2003, *ApJ*, **592**, 906
- Iwamoto K., Brachwitz F., Nomoto K., Kishimoto N., Umeda H., Hix W. R., Thielemann F.-K., 1999, *ApJS*, **125**, 439
- Jeena S. K., Banerjee P., Chiaki G., Heger A., 2023, *MNRAS*, **526**, 4467
- Jeena S. K., Banerjee P., Heger A., 2024, *MNRAS*, **527**, 4790
- Khokhlov A. M., 1991, *A&A*, **245**, 114
- Kirby E. N., et al., 2019, *ApJ*, **881**, 45
- Kobayashi C., Leung S.-C., Nomoto K., 2020, *ApJ*, **895**, 138
- Lach F., Röpke F. K., Seitenzahl I. R., Côté B., Gronow S., Ruiter A. J., 2020, *A&A*, **644**, A118
- Leung S.-C., Nomoto K., 2018, *ApJ*, **861**, 143
- Leung S.-C., Nomoto K., 2020, *ApJ*, **888**, 80
- Li H., et al., 2022, *ApJ*, **931**, 147
- Magg M., et al., 2020, *MNRAS*, **498**, 3703
- Marino A. F., et al., 2019, *MNRAS*, **485**, 5153
- McWilliam A., Piro A. L., Badenes C., Bravo E., 2018, *ApJ*, **857**, 97
- Müller B., et al., 2019, *MNRAS*, **484**, 3307

- Nomoto K., Thielemann F. K., Yokoi K., 1984, [ApJ](#), 286, 644
- Placco V. M., Frebel A., Beers T. C., Stancliffe R. J., 2014, [ApJ](#), 797, 21
- Rauscher T., Heger A., Hoffman R. D., Woosley S. E., 2002, [ApJ](#), 576, 323
- Rauscher T., Heger A., Hoffman R. D., Woosley S. E., 2003, [Nuclear Phys. A](#), 718, 463
- Reggiani H., Schlaufman K. C., Casey A. R., 2023, [AJ](#), 166, 128
- Seitenzahl I. R., et al., 2013a, [MNRAS](#), 429, 1156
- Seitenzahl I. R., Cescutti G., Röpke F. K., Ruiter A. J., Pakmor R., 2013b, [A&A](#), 559, L5
- Shen K. J., Kasen D., Miles B. J., Townsley D. M., 2018, [ApJ](#), 854, 52
- Sieverding A., Müller B., Qian Y. Z., 2020, [ApJ](#), 904, 163
- Skúladóttir Á., Koutsouridou I., Vanni I., Amarsi A. M., Lucchesi R., Salvadori S., Aguado D. S., 2024, [ApJ](#), 968, L23
- Thibodeaux P. N., Ji A. P., Cerny W., Kirby E. N., Simon J. D., 2024, [arXiv e-prints](#), p. [arXiv:2404.17078](#)
- Tominaga N., Umeda H., Nomoto K., 2007, [ApJ](#), 660, 516
- Tominaga N., Iwamoto N., Nomoto K., 2014, [ApJ](#), 785, 98
- Umeda H., Nomoto K., 2003, [Nature](#), 422, 871
- Umeda H., Nomoto K., 2005, [ApJ](#), 619, 427
- Wang T., Burrows A., 2024, [ApJ](#), 962, 71
- Weaver T. A., Zimmerman G. B., Woosley S. E., 1978, [ApJ](#), 225, 1021
- Woosley S. E., Kasen D., 2011, [ApJ](#), 734, 38
- Woosley S. E., Taam R. E., Weaver T. A., 1986, [ApJ](#), 301, 601
- Woosley S. E., Heger A., Weaver T. A., 2002, [Reviews of Modern Physics](#), 74, 1015
- Xing Q.-F., et al., 2023, [Nature](#), 618, 712
- de los Reyes M. A. C., Kirby E. N., Seitenzahl I. R., Shen K. J., 2020, [ApJ](#), 891, 85